

THE STELLAR STRUCTURE AND KINEMATICS OF DWARF SPHEROIDAL GALAXIES FORMED BY TIDAL STIRRING

EWA L. LOKAS¹, STELIOS KAZANTZIDIS^{2,3,4}, JAROSŁAW KLIMENTOWSKI¹,
LUCIO MAYER^{5,6}, AND SIMONE CALLEGARI⁵

The Astrophysical Journal, accepted

ABSTRACT

Using high-resolution N -body simulations we study the stellar properties of dwarf spheroidal (dSph) galaxies resulting from the tidally induced morphological transformation of disk dwarfs on a cosmologically motivated eccentric orbit around the Milky Way. The dwarf galaxy models initially consist of an exponential stellar disk embedded in an extended spherical dark matter halo. Depending on the initial orientation of the disk with respect to the orbital plane, different final configurations are obtained. The least evolved dwarf is triaxial and retains a significant amount of rotation. The more evolved dwarfs are prolate spheroids with little rotation. We show that in this scenario the final density distribution of stars can be approximated by a simple modification of the Plummer law. The kinematics of the dwarfs is significantly different depending on the line of sight which has important implications for mapping the observed stellar velocity dispersions of dwarfs to subhalo circular velocities. When the dwarfs are observed along the long axis, the measured velocity dispersion is higher and decreases faster with radius. In the case where rotation is significant, when viewed perpendicular to the long axis, the effect of minor axis rotation is detected, as expected for triaxial systems. We model the velocity dispersion profiles and rotation curves of the dwarfs under the assumption of constant mass-to-light ratio by solving the Jeans equations for spherical and axisymmetric systems and adjusting different sets of free parameters, including the total mass. We find that the mass is typically overestimated when the dwarf is seen along the long axis and underestimated when the observation is along the short or intermediate axis. For the studied cases the effect of non-sphericity cannot however bias the inferred mass by more than 60 percent in either direction, even for the most strongly stripped dwarf which is close to disruption.

Subject headings: galaxies: dwarf – galaxies: fundamental parameters – galaxies: kinematics and dynamics – galaxies: Local Group – galaxies: structure – cosmology: dark matter

1. INTRODUCTION

Dwarf spheroidal (dSph) galaxies of the Local Group (for a review see Mateo 1998) can provide crucial tests of the currently favored cold dark matter (CDM) paradigm of cosmological structure formation (e.g., White & Rees 1978; Blumenthal et al. 1984). Several scenarios have been proposed so far for the origin of these systems, including gravitational interactions in the form of galaxy harassment (e.g., Moore et al. 1996) tidal stirring (Mayer et al. 2001; Kravtsov et al. 2004; Kazantzidis et al. 2004b) or resonant stripping (D’Onghia et al. 2009) as well as hydrodynamical processes (e.g., Ricotti & Gnedin 2005; Mayer et al. 2007; Tassis et al. 2008). The tidal stirring scenario proposed by Mayer et al. (2001, see also Gnedin et al. 1999; Peñarrubia et al. 2008) can explain the morphological transformation of disk dwarf galaxies resembling dwarf irregulars into pressure-supported

stellar systems with the structural properties of dSphs. When combined with ram pressure stripping and the effect of the UV background (Bullock et al. 2000; Susa & Umemura 2004) it can also account for the low gas content and the very high mass-to-light ratios (M/L) of some of them (Mayer et al. 2006; 2007).

In order to explore this scenario in more detail Klimentowski et al. (2007, 2009a) have recently studied the evolution of two-component dwarf galaxies orbiting the Milky Way on a cosmologically motivated eccentric orbit using high resolution N -body simulations. The dwarfs were initially composed of a stellar disk embedded in a more extended dark matter halo. Three simulations were performed which differed by the initial inclination of the disk with respect to the orbital plane. Although the evolution proceeded a little differently in each case, strong mass loss and morphological transformation of the disk always took place. After the first or second (out of five) pericenter passages the disk evolves into a bar which in the subsequent evolution becomes shorter. The morphological transformation of the stellar component is accompanied by the loss of angular momentum so that little rotation remains at the end. The final products are very similar in shape to the dSph galaxies of the Local Group. In this paper we study in detail the structural and kinematic properties of stars in these dwarfs at the end of their tidal evolution.

dSph galaxies are also interesting because of their significant dark matter content. It turns out that the tidal

¹ Nicolaus Copernicus Astronomical Center, Warsaw, Poland; lokas@camk.edu.pl

² Center for Cosmology and Astro-Particle Physics, The Ohio State University, Columbus, OH 43210, USA; stelios@mps.ohio-state.edu

³ Department of Physics, The Ohio State University, Columbus, OH 43210, USA

⁴ Department of Astronomy, The Ohio State University, Columbus, OH 43210, USA

⁵ Institute for Theoretical Physics, University of Zürich, CH-8057 Zürich, Switzerland; lucio@phys.ethz.ch

⁶ Institute of Astronomy, Department of Physics, ETH Zürich, CH-8093 Zürich, Switzerland

TABLE 1
PROPERTIES OF THE SIMULATED DWARFS.

simulation	i [deg]	r_{\max} [kpc]	$M_{\text{tot}}(r_{\max})[M_{\odot}]$	$N_{\text{stars}}(r_{\max})$	$N_{\text{DM}}(r_{\max})$	$M_{\text{stars}}(r_{\max})[M_{\odot}]$	$M_{\text{DM}}(r_{\max})[M_{\odot}]$
A	90	2.00	3.73×10^7	73423	25394	1.10×10^7	2.63×10^7
B	45	1.70	2.05×10^7	37739	14378	5.64×10^6	1.49×10^7
C	0	1.44	4.67×10^6	8379	3298	1.25×10^6	3.42×10^6

stirring scenario is able to reproduce both the mildly dark matter dominated dwarfs like Fornax or Leo I (Klimontowski et al. 2007, 2009a) and the very dark ones like Draco (Mayer et al. 2007). In spite of significant mass loss due to tidal stripping the dwarfs are able to retain enough dark matter to remain mostly dark, although the extended dark halo is lost very fast and the mass approximately traces light in the final stages. This means that according to this scenario the mass modeling of dSph galaxies can be reliably done adopting the scale lengths of the distribution of light as is indeed a common approach.

The presence of tidal stripping however also means that in addition to the contamination from Milky Way stars, which can be dealt with using photometric methods (Majewski et al. 2000) or metallicities (Walker et al. 2009a), the kinematic samples used for dynamical modeling can be contaminated by tidal debris. Klimontowski et al. (2009b) have shown that such contamination is indeed very probable because of the typically radial orientation of tidal tails for dwarfs on eccentric orbits. This contamination may artificially inflate the velocity dispersion and bias the inferred parameters of the density profile or the anisotropy of stellar orbits. It can however be reliably removed using procedures for interloper rejection (Klimontowski et al. 2007; Lokas et al. 2008).

Another source of systematic error in the dynamical modeling may be due to departures from sphericity. As mentioned above, the products of tidal stirring are not spherical but rather form prolate spheroids. In this work we study the effect of non-sphericity on mass and anisotropy estimates, i.e. we show what biases are expected if spherical models are applied to galaxies whose shapes depart from spherical. We also discuss how the estimates can improve if axisymmetric models are used in those cases where rotation is detected.

The paper is organized as follows. In section 2 we provide a brief description of the simulations used in this work. In section 3 we study the properties of the stellar component of three dSph galaxy models obtained in three simulations with different initial inclination of the disk. Section 4 discusses the line-of-sight density and velocity distributions, as they would be seen by a distant observer. In section 5 we briefly compare the properties of our simulated dwarfs to observations. Section 6 is devoted to modeling the mock kinematic data using spherical and axisymmetric models and studying the biases inherent in such modeling for different lines of sight. The discussion follows in section 7.

2. THE SIMULATIONS

The simulations used for the present study follow the evolution of dwarf disk-like systems orbiting within the static host potential of a Milky Way-sized galaxy and are described in detail in Klimontowski et al. (2007, 2009a).

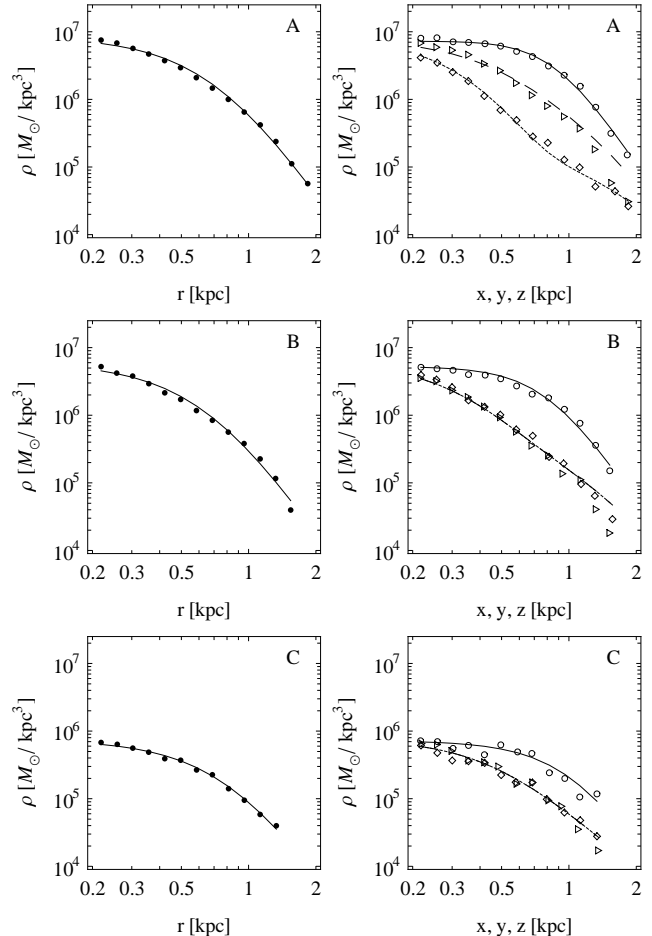


FIG. 1.— Density distributions of stars in the simulated dwarfs. The first, second and third row corresponds respectively to dwarf A, B and C of Table 1. The left column panels show the density distribution of stars measured in radial bins (filled circles) and the solid lines show the Plummer law (1) with parameters from Table 2 fitted to the data. The second column presents the densities measured in narrow cuboids along the x (circles), y (triangles) and z (squares) axis of the dwarfs. The solid, dashed and dotted lines show respectively the best-fitting profiles obtained with density following from the potential (3) with parameters listed in Table 3.

Here we provide a short summary of the most important parameters. Live dwarf galaxy models are constructed using the technique by Hernquist (1993) and consist of an exponential stellar disk embedded in a spherical and isotropic Navarro et al. (1996, hereafter NFW) dark matter halo. The structural properties of the dark halo and disk are related through disk galaxy formation models in the currently favored concordance CDM cosmological model (Mo et al. 1998).

The dwarf progenitor has the total mass $M = 4.3 \times 10^9 M_{\odot}$. The mass and radial scale length of the disk are $1.5 \times 10^8 M_{\odot}$ and $R_d = 1.3$ kpc, respectively, and its

TABLE 2
FITTED PARAMETERS OF THE SPHERICAL MODELS FOR THE
DISTRIBUTION OF STARS.

simulation	$M_s [M_\odot]$	a [kpc]
A	1.33×10^7	0.73
B	7.01×10^6	0.66
C	2.00×10^6	0.86

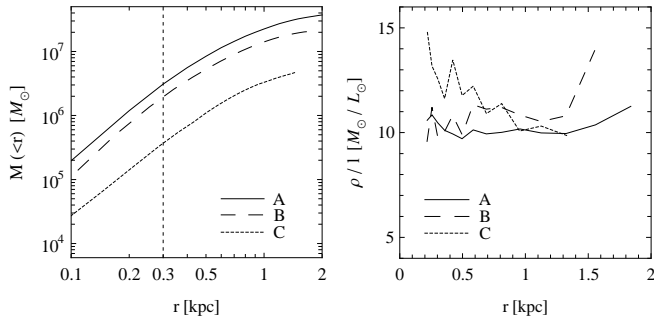


FIG. 2.— Left panel: the final mass profiles of the three simulated dwarfs A, B and C (solid, dashed and dotted line respectively). The vertical dashed line indicates the values of mass within 300 pc, M_{300} . Right panel: the final mass-to-light density ratios for the three dwarfs.

vertical structure is modeled by isothermal sheets (with the vertical scale height $z_d = 0.13$ kpc). The halo virial mass and concentration are $M_{\text{vir}} = 3.7 \times 10^9 M_\odot$ and $c = 15$, respectively. The halo is exponentially truncated outside the virial radius $r_{\text{vir}} \simeq 40.2$ kpc to keep the total mass finite (Kazantzidis et al. 2004a) and adiabatically contracted in response to the growth of the disk (Blumenthal et al. 1986). The host galaxy is modeled by a static gravitational potential based on the dynamical mass model A1 for the Milky Way (Klypin et al. 2002). It consists of a NFW halo with the virial mass of $M_{\text{vir}} = 10^{12} M_\odot$ and concentration $c = 12$, a stellar disk with mass $M_D = 4 \times 10^{10} M_\odot$, the scale length $R_d = 3.5$ kpc and the scale height $z_d = 0.35$ kpc, and a bulge of mass $M_b = 0.008 M_{\text{vir}}$ and scale-length $a_b = 0.2 R_d$. The dwarf galaxy evolves on an eccentric orbit with apocenter $r_a = 120$ kpc and pericenter to apocenter ratio of $r_p/r_a \approx 0.2$, close to the median ratio of pericentric to apocentric radii found in high-resolution cosmological N -body simulations (Ghigna et al. 1998; Diemand et al. 2007). The evolution is followed for 10 Gyr corresponding to approximately five orbital times. We used three simulations with the disk initially inclined by 0° , 45° , and 90° with respect to the orbital plane.

Lastly, the simulations were performed using PKDGRAV, a multisteping, parallel, tree N -body code (Stadel 2001). We sampled the live dwarf galaxy with 4×10^6 dark matter particles and 10^6 stellar particles, and employed a gravitational softening length of 100 and 50 pc, respectively.

3. THE PRODUCTS OF TIDAL STIRRING

Table 1 lists the basic properties of the simulated dwarfs in the final stage. For a detailed description of the intermediate evolution we refer the reader to Klimentowski et al. (2009a). In order to avoid any contamination from the tidally disrupted stars we select only the

TABLE 3
FITTED PARAMETERS OF THE NON-SPHERICAL MODELS FOR THE
DISTRIBUTION OF STARS.

simulation	$M_s [M_\odot]$	a [kpc]	b [kpc]	c [kpc]	d [kpc]
A	1.62×10^7	0.83	0.93	0.81	1.41
B	8.74×10^6	0.76	0.74	1.16	1.16
C	2.70×10^6	1.02	0.77	1.22	1.22

stellar and dark matter particles within radius $r < r_{\text{max}}$ kpc from the center of the dwarf. The adopted values of r_{max} , listed in the Table, were determined by inspection of the stellar density profiles, i.e. they are the radii at which the profiles start to flatten signifying the transition to the tidal tails. The radii are of the order of the dwarf’s tidal radius or slightly smaller. The Table also gives the initial inclinations of the stellar disk plane with respect to the orbital plane, the total masses of the dwarfs within r_{max} , the numbers of stars and dark particles contained inside these radii and the stellar and dark masses separately. In section 5 we discuss the observational properties of our dwarfs.

The left column of Figure 1 shows with the filled circles the radially averaged density profile of the stars in the three simulated dwarfs measured in the range between $r = 0.2$ kpc (which is larger than our resolution limit) and $r = r_{\text{max}}$ in logarithmic bins. The data are well fitted by the Plummer distribution

$$\rho(r) = \frac{3a^2 M_s}{4\pi} \frac{1}{(r^2 + a^2)^{5/2}}, \quad (1)$$

where M_s is the total mass of the stellar component and a is the characteristic scale-length. This density follows via the Poisson equation from the potential

$$\Phi(r) = -\frac{GM_s}{(r^2 + a^2)^{1/2}}. \quad (2)$$

The fits were done by minimizing the sum $\sum_i (\rho_{\text{data}} - \rho_{\text{model}})^2 / \rho_{\text{model}}^2$. The best-fitting profiles are plotted as solid lines in the left-column panels of Figure 1 and the best-fitting parameters are listed in Table 2. The corresponding half-light radii are $r_{1/2} = 1, 0.9$ and 1.15 kpc respectively for model A, B and C.

In order to describe the departures from sphericity in the structure of the dwarfs using the stellar particles we determine the principal axes of the inertia tensor and define our coordinate system so that the x axis lies along the longest axis of the stellar distribution and the z axis along the shortest. We measure the density along the x , y and z axis in cuboids of logarithmic bins along the given axis and of ± 0.2 kpc width along the remaining dimensions, so for example for the measurements along the z axis we adopt $|x| < 0.2$ kpc and $|y| < 0.2$ kpc. The measurements were made along the positive and negative side of a given axis and then averaged.

The density profiles measured along the three axes (ρ are shown in the right column of Figure 1 with circles corresponding to the measurements along the x axis, triangles along the y axis and squares along z). We see that the shape of model A is clearly triaxial: the densities are significantly different along the three axes: the distribution is rather flat along the x axis signifying the presence of a remnant bar and very steep (almost a power law)

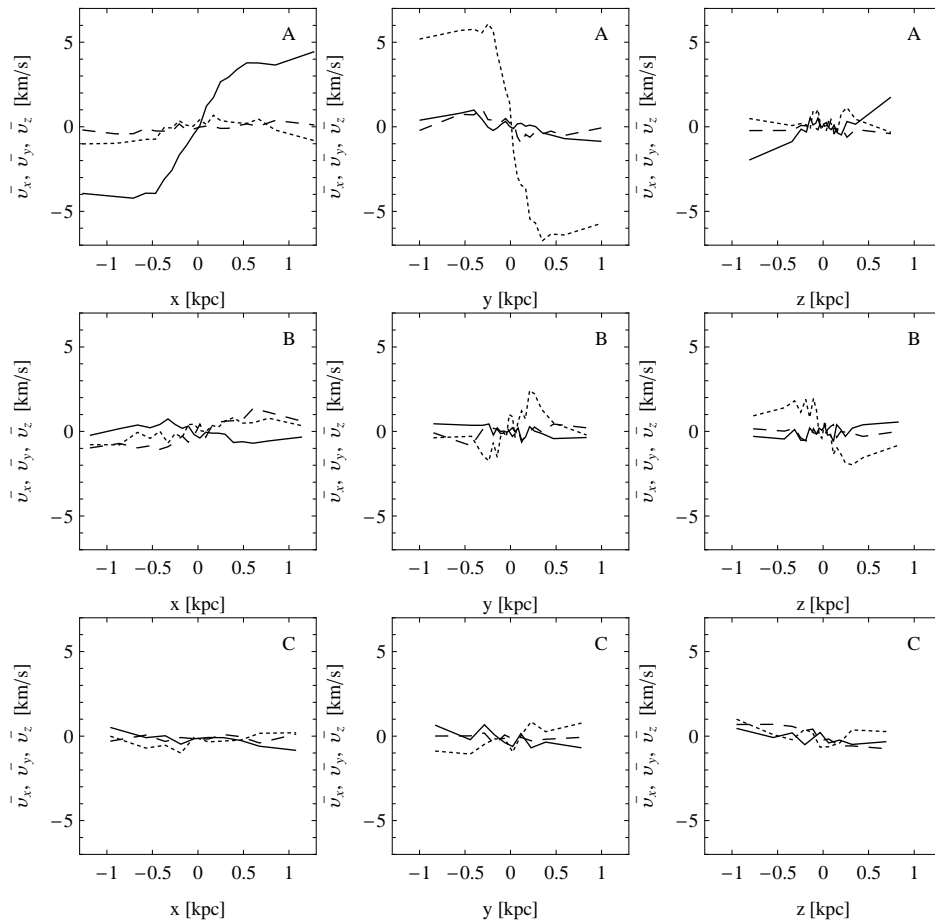


FIG. 3.— Mean velocities along the three axes $\overline{v_x}$ (dotted line), $\overline{v_y}$ (solid line) and $\overline{v_z}$ (dashed line) as a function of x , y and z (left to right column). The three rows show results for dwarf A, B and C respectively.

along the z axis. As we demonstrate below, the z axis almost coincides with the rotation axis of the dwarf. This means that in addition to the presence of the remnant bar, dwarf A is also flattened due to rotation.

The shapes of the models B and C are spheroidal, i.e. the density distribution is rather flat along the x axis and steeper along y and z but the latter two profiles are indistinguishable (therefore our choice of y and z is random with respect to x). Note also that the distribution of stars in model C is noisier, the dwarf is irregular and close to disruption, as indicated by its much smaller mass (see Table 1).

The density distribution along the three axes can be well approximated by the density following by the Poisson equation from the modified Plummer potential

$$\Phi(x, y, z) = \frac{GM_s}{[(x^2 + y^2 + z^2 + a^2)^2 - b^2x^2 + c^2y^2 + d^2z^2]^{1/4}} \quad (3)$$

where again M_s is the total mass while a, b, c and d are constants with the dimension of length. The first term in the denominator is the same as in the original Plummer potential, $(r^2 + a^2)$. The second, negative term, $-b^2x^2$, introduces a bar-like distribution along the x axis and the third and fourth positive terms c^2y^2 and d^2z^2 , make the profile steeper along the y and z axis respectively. The form of the potential (3) is a generalization of the modified Plummer distribution proposed by Lynden-Bell

(1962).

We fitted the profiles measured from the simulation with the density following from (3) via the Poisson equation by the same minimization scheme, except that now the data points for model A were weighted by the density measured along the y axis which have intermediate values (otherwise the measurements along the z axis would be fitted best). For models B and C the data points were weighted by the average value of density along x and y . The solid, dashed and dotted lines in the second column of Figure 1 show respectively the best-fitting profiles along the x , y and z axis respectively, obtained with parameters listed in Table 3. Note that for models B and C we kept $c = d$.

The important dynamical properties of the three simulated dwarfs are illustrated further in Figure 2. This figure shows the final mass, $M(< r)$, and mass-to-light density, ρ/l , profiles plotted up to each corresponding r_{\max} . It can immediately be seen that the mass profiles are very different in spite of the fact that the three dwarfs had identical initial density distributions and orbits and differed only by the initial inclination of the disk with respect to the orbital plane. Interestingly, while our dwarfs started with identical masses within 300 pc, M_{300} , they become substantially different among the three final models being almost an order of magnitude larger in dwarf A compared to that of dwarf C.

Figure 2 also shows that the final mass-to-light den-

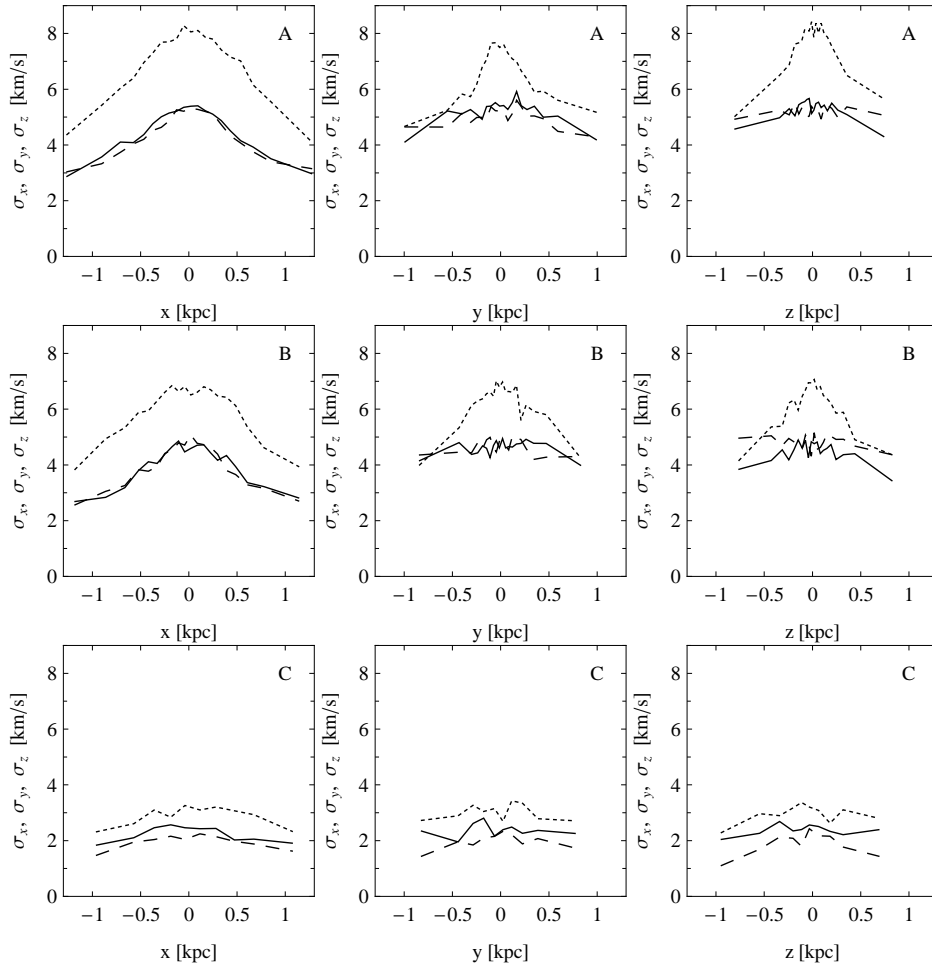


FIG. 4.— Dispersions of the velocities along the three axes σ_x (dotted line), σ_y (solid line) and σ_z (dashed line) as a function of x , y and z (left to right column). The three rows show results for dwarf A, B and C respectively.

sity ratios are not significantly different among the three dwarfs and, in addition, they are all almost constant with radius. The former is related to the fact that the initial mass-to-light distributions were identical and indicates that the dark matter and stars are lost in proportional amounts in all cases. The latter is a consequence of two facts. First, the initial mass-to-light distributions were constant within ~ 2 kpc or so (Klimentowski et al. 2007). Second, after the outer part of the dark matter halo, which was initially much more extended than the stars, is stripped at the first pericenter passage, the stars and dark matter are stripped from all radii. Note that a similar result is obtained in simulations including gas dynamics (Mayer et al. 2007). The final mass-to-light profile could however be different if other initial conditions were assumed (e.g. Peñarrubia et al. 2008).

The velocity distribution of the stellar components of the dwarfs is illustrated in Figures 3 and 4. In Figure 3 we plot the mean velocities along the three axes, $\overline{v_x}$, $\overline{v_y}$ and $\overline{v_z}$ as a function of x , y and z . As in the case of density, the measurements were made in narrow cuboids placed along a given axis, e.g. for the measurements as a function of z we selected stars with $|x| < 0.2$ kpc and $|y| < 0.2$ kpc. For model A significant rotation can be seen, but mostly in the xy plane, i.e. much less rotation is seen along z . For model B rotation is very small and

for model C negligible. This can be understood as due to more effective removal of angular momentum for models where the stars initially had angular momentum more aligned with the orbital angular momentum of the dwarf (e.g., Read et al. 2006).

Figure 4 shows the velocity dispersion profiles along the three axes σ_x , σ_y and σ_z as a function of x , y and z . Here and below the dispersions are measured with respect to the mean velocity in a given bin and calculated using the unbiased estimator $s = [\sum_{i=1}^n (v_i - \overline{v})^2 / (n - 1)]^{1/2}$ where n is the number of stars in a bin. We can see that the velocity dispersions along x are always largest, while those along y and z are smaller and comparable to each other.

4. THE LINE-OF-SIGHT DISTRIBUTIONS

In this section we discuss the line-of-sight distributions of density and velocity of the stars which can be directly compared to observations. The triaxiality of dwarf A is further illustrated in Figure 5 where we plot the surface density distributions of the stars seen along the three axes x , y and z from the top to the bottom row. The left column panels show the isodensity contours of the surface density measured from the simulation and the right column panels the corresponding values from the best-fitting model following from the modified Plummer

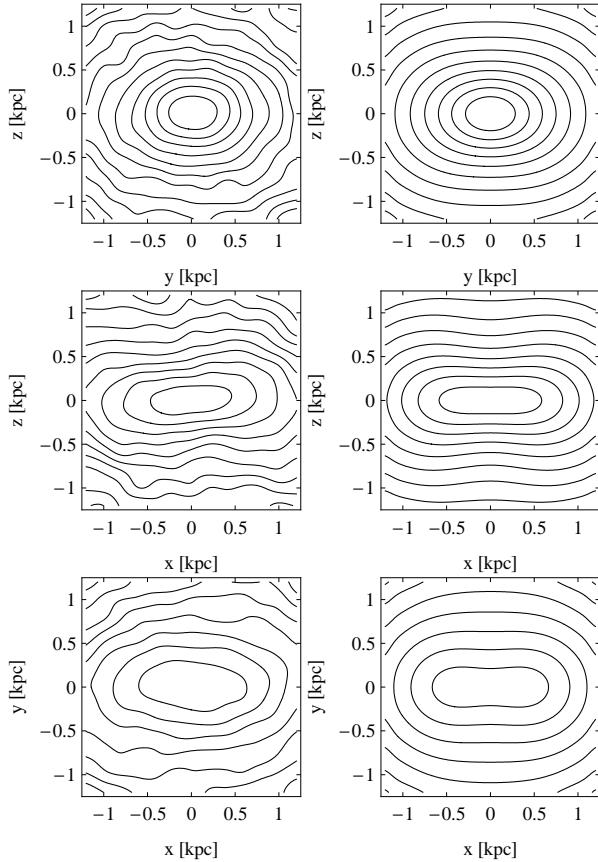


FIG. 5.— Surface mass distribution of the stellar component of dwarf A observed along the x , y and z axis (from the upper to the lower row). Left panels show the contours of equal surface density of stars measured from the simulation. Right panels plot the corresponding distributions of the modified Plummer model (3) with parameters from Table 3 adjusted to the density profiles in Figure 1. The surface densities Σ were expressed in $M_{\odot} \text{ kpc}^{-2}$ and the contours are spaced by $\Delta \log \Sigma = 0.2$. The innermost contour level is $\log \Sigma = 7$ (upper row), 6.8 (middle row) and 6.6 (lower row).

potential (3) with parameters from Table 3. We see that the model reproduces quite well the basic features of the simulated dwarf. When viewed along the z axis (lower row) the remnant bar is well visible but there is otherwise little flattening. When viewed along the y axis (middle row), both the bar and the flattening along z are well visible. When viewed along the x axis (upper row) the bar is not seen, the contours are almost circular except for some flattening along the z axis.

Figures 6 and 7 present analogous results for models B and C, except that now we show only the view along the longest axis (upper row) and along one of the other two axes (lower row) since the two look very similar. As expected for spheroidal shapes, the surface density contours for the view along the x axis are circular. In the perpendicular direction an elongated shape is seen. The two models look quite similar, although model B is more massive (see the different contour levels), except for the fact that in the case of model C the contours are much more irregular, which is a sign of a stage close to disruption.

Figure 8 illustrates the line-of-sight kinematics of the stars in the simulated dwarfs. The measurements are

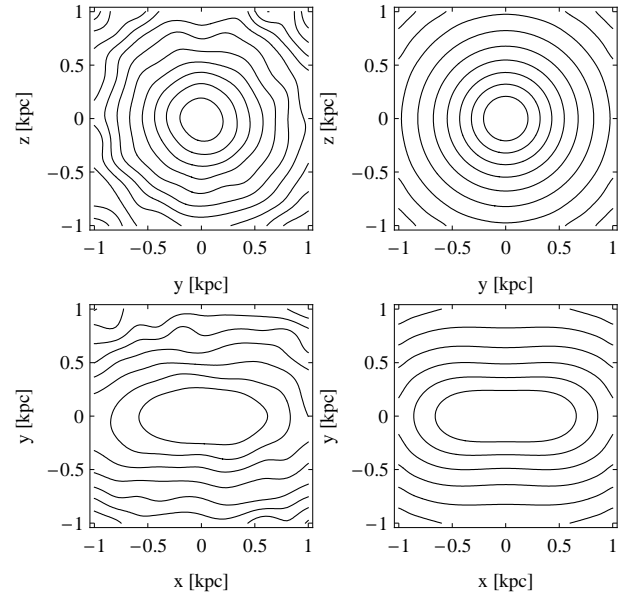


FIG. 6.— Surface mass distribution of the stellar component of dwarf B observed along the x axis (upper row) and perpendicular to it (lower row). Left panels show the contours of equal surface density of stars measured from the simulation. Right panels plot the corresponding distributions of the modified Plummer model (3) with parameters from Table 3 adjusted to the density profiles in Figure 1. The surface densities Σ were expressed in $M_{\odot} \text{ kpc}^{-2}$ and the contours are spaced by $\Delta \log \Sigma = 0.2$. The innermost contour level is $\log \Sigma = 6.8$ (upper row) and 6.4 (lower row).

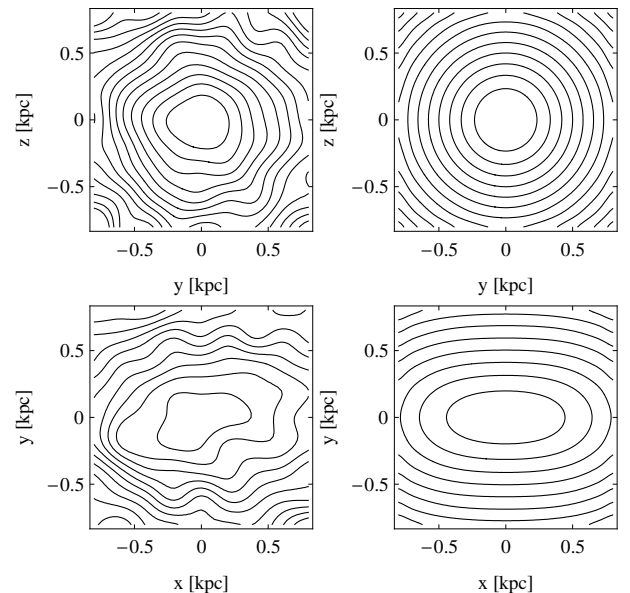


FIG. 7.— The same as Figure 6 but for dwarf C. The contour spacing is $\Delta \log \Sigma = 0.1$ and the innermost contour level is $\log \Sigma = 6$ (upper row) and 5.8 (lower row).

done in the same configuration as for the surface density in Figures 5-7. Note that no clipping of the data is necessary since we still consider only stars within r_{max} . The columns from the left to the right correspond to observations along the x , y and z axis. The first row shows the contours of equal line-of-sight velocity and the second row the contours of equal line-of-sight velocity dispersion for model A. Next rows present analogous measure-

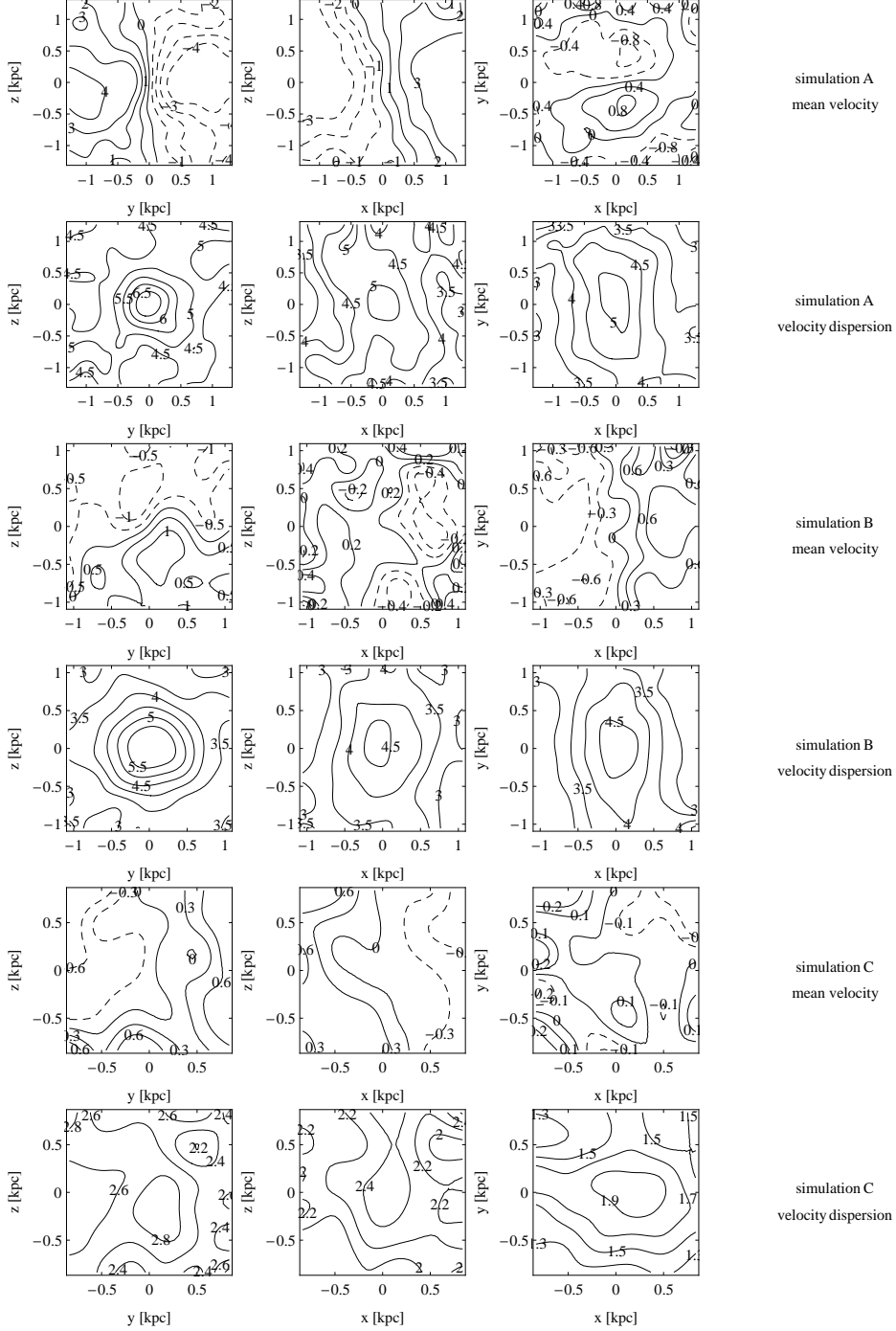


FIG. 8.— Line-of-sight kinematics of the stellar component observed along the x , y and z axis (from the left to the right column). The first and second row present the mean velocity and velocity dispersion maps respectively, for the dwarf in simulation A. The subsequent rows show the results for simulations B and C as marked on the right hand side of the Figure. Contour levels in km s^{-1} are indicated in each panel. Contours of negative mean velocity are shown with dashed lines. The measurements were made by binning the data in cells of size 0.28, 0.3 and 0.33 kpc respectively for simulation A, B and C respectively.

ments for models B and C. Contour levels of the quantities expressed in km s^{-1} are marked in each panel and the dashed contour lines indicate negative values.

Again, for model A rotation is well visible when the observation is along the x axis (left column) and along y axis (middle column) while it is much smaller for the line of sight along the z axis (right column). The velocity dispersions are similar for the observations along z and y while the dispersion measured along the longest axis is larger and decreases more steeply with distance from the

center of the dwarf. A similar steeper decline of velocity dispersion along the longest axis is seen for model B, but the rotation level is low in this case. For model C the dispersion is rather flat even along the longest axis and rotation is very low.

The velocity structure seems to be the richest in the case of model A, as expected for triaxial systems. Figures 3 and 8 show that the orbital structure of our simulated dwarfs is similar to the one found for simple triaxial models corresponding to Stäckel potentials (de Zeeuw

TABLE 4
OBSERVATIONAL PROPERTIES OF THE SIMULATED DWARFS.

simulation	M_V	μ_V [mag/arcsec ²]	$r_{1/2}$ [kpc]	σ_0 [km s ⁻¹]	V/σ
A	-11.8	25.8-24.7	0.53-0.88	5-6.5	0.16-0.62
B	-11.1	26.0-25.2	0.47-0.74	4.5-5.5	0.09-0.18
C	-9.7	27.9-27.4	0.73-0.98	1.9-2.8	0.11-0.25

1985; Statler 1987). For such models four families of orbits are identified: box orbits, short-axis tube orbits and inner and outer long-axis tube orbits. The only orbits with net angular momentum circulate either around the short or the long axis in agreement with the rotation curves shown in Figure 3. The total angular momentum is thus generally misaligned from the short axis which results in a velocity gradient along the apparent minor axis when the galaxy is observed in projection. This means that the zero velocity curve is misaligned with the minor axis, as we indeed see in the middle panel of the upper row of Figure 8 (observation along y). The rotation is however much stronger around the short axis. For prolate spheroids (models B and C) only the long-axis tubes are allowed but since the rotation levels are low in these cases the stars must travel in both directions so that no single (clockwise or anti-clockwise) direction dominates.

5. COMPARISON WITH OBSERVATIONS

To summarize the properties of the simulated dwarfs described in the two previous sections, in Table 4 we provide the basic parameters that can be directly compared to observations. The visual magnitudes M_V were calculated from the total stellar mass of the models assuming the stellar $M/L_V = 3 M_\odot/L_\odot$. For the remaining quantities, the central surface brightness μ_V , the half-light radius $r_{1/2}$, central velocity dispersion σ_0 and the ratio of the rotation velocity to the velocity dispersion V/σ we provide ranges of values corresponding to different lines of sight (along x , y and z). The values of V/σ were calculated by taking the maximum line-of-sight rotation and dispersion measured along the major or minor axis of the galaxy, as in Figure 8.

Comparison with the observed values of these parameters for the Local Group dSph galaxies (e.g. Mateo 1998; Grebel et al. 2003; Tolstoy et al. 2009) shows that they are rather representative for this type of objects. Only the velocity dispersion values may appear a little too low. Note however, that we have considered here the final stages of the evolution, i.e. after 10 Gyr when the dwarfs have lost majority of their mass. Although the progenitors of dSph galaxies are expected to become satellites early, not all such galaxies have been tidally stripped for so long. Moving back 2 or 4 Gyr in our simulations we would easily find earlier stages with velocity dispersions 50-100 percent higher but other properties very similar (see section 4 and fig. 12 in Klimentowski et al. 2009a).

The parameters in Table 4 also obey the relationships like $M_V - \mu_V$ or $M_V - r_{1/2}$, i.e. in plots showing these relations (such as fig. 34 in Kormendy et al. 2009 or fig. 1 in Tolstoy et al. 2009) our dwarfs would occupy regions characteristic of dSph galaxies. Although with just three cases considered we cannot really explore cor-

relations between the parameters, we can immediately see that there is a clear trend of surface brightness decreasing with decreasing luminosity as observed in real dSph galaxies, in contrast to ellipticals (fig. 1 in Kormendy et al. 2009). This feature, among others, has been interpreted as pointing towards different formation scenarios of spheroidal and elliptical galaxies by Kormendy (1985) and Kormendy et al. (2009). They suggested that elliptical galaxies may form mostly via mergers while spheroidals are rather late-type systems that underwent transformation due to star-formation processes or environmental effects such as tidal stirring. This idea has recently gained support from the theoretical side; based on the analysis of the simulated Local Group Klimentowski et al. (2009c) found that mergers of subhaloes are quite rare in such systems and occur early on so they cannot significantly contribute to the formation of a large fraction of dSph galaxies. The tidal stirring scenario thus seems to be the most effective gravitational mechanism by which such objects could form.

Although our initial conditions constitute just one possible model for the progenitors of dSphs, our results suggest that tidal interactions with the primary alone may introduce an appreciable scatter in M_{300} (see Figure 2), which could lead to some tension with claims of a common mass scale for Galactic satellites within 300 pc (Strigari et al. 2008). In addition, while we cannot exclude the effects of baryonic physics on our findings, one could expect that a wider spectrum of initial conditions and orbits would likely further differentiate the inner masses of dSph galaxies.

Recently, Walker et al. (2009c) suggested instead the existence of a scaling relation for dSph galaxies between the half-light radius and the mass contained within it of the form $M(r_{1/2})/M_\odot = 5800(r_{1/2}/\text{pc})^{1.4}$. The masses $M(r_{1/2})$ of our dwarfs (in units of $10^7 M_\odot$) are within the ranges 0.94-2, 0.52-1 and 0.22-0.33 (depending on the line of sight) respectively for dwarfs A, B and C. Combining with the half-light radii from Table 4 we find that our dwarfs fall below the line proposed by Walker et al., i.e. for these half-light radii they have smaller masses than the relation would predict. Note however that the masses used by Walker et al. may be overestimated due to contamination. With just three cases considered here (including one close to disruption) we cannot fully address the issue and we defer such investigations to future work.

6. THE EFFECT OF NON-SPHERICITY ON MASS ESTIMATES

6.1. Velocity moments and the Jeans equations

In order to further study the observational consequences of non-sphericity of dSph galaxies we now attempt to model the kinematics of our simulated dwarfs. For each of the characteristic lines of sight discussed

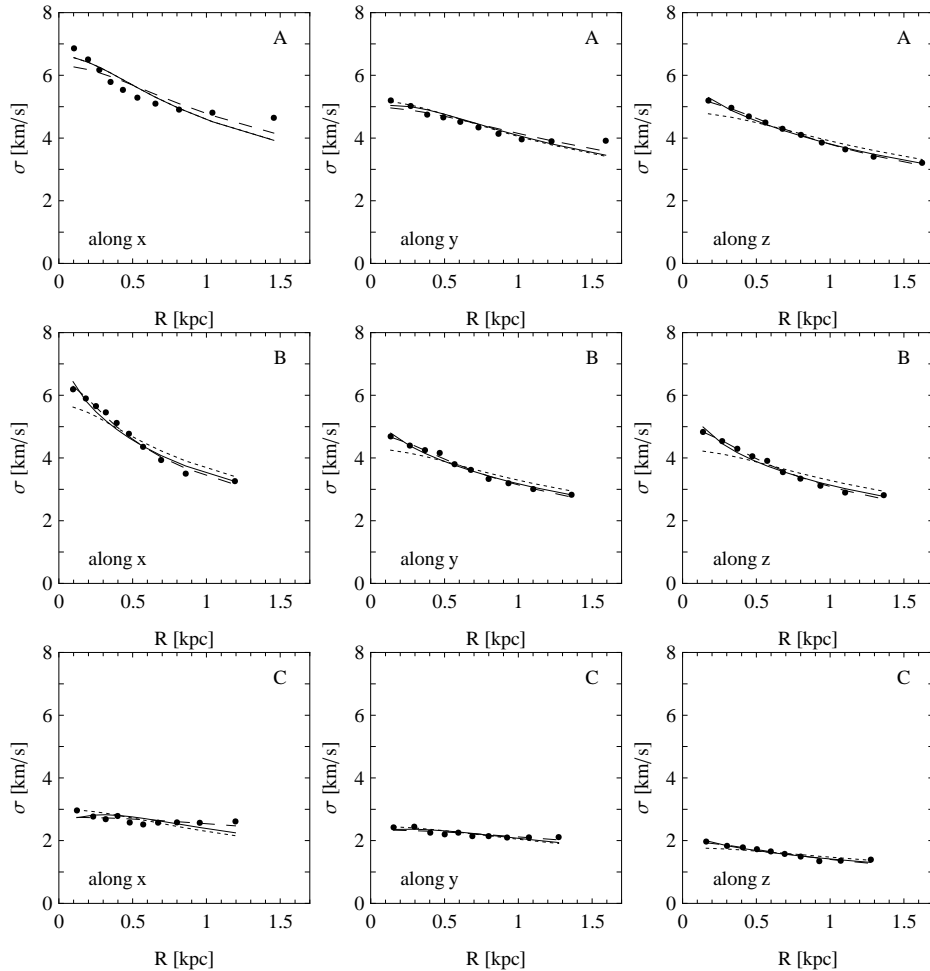


FIG. 9.— Line-of-sight velocity dispersion profiles as a function of the projected radius R for dwarfs obtained in simulation A, B and C (from the upper to the lower row) for the observation along the x , y and z axis (from the left to the right column). The dotted lines show the best fitting isotropic ($\beta = 0$) solutions of the Jeans equation for the one-component model with scale length a adopted from the fit of the surface density of stars (Table 5 and Figure 12) and only the mass M adjusted. The solid lines are for models with a assumed and M and anisotropy β fitted. The dashed lines show the best-fitting isotropic models with M and a adjusted. In the upper left panel the dotted line coincides with the solid one. The best-fitting parameters are listed in Table 6.

above, i.e. along the x , y and z axis, we measure the rotation velocity V and the velocity dispersion σ along the line of sight. For this purpose we use all the available stars although in real observations the presently available samples are at least an order of magnitude less numerous. We are however more interested here in studying systematic errors in the estimated parameters rather than estimating their realistic statistical errors. We assign to the measured values of the velocity moments the true sampling errors which are used to weigh the data points when fitting. Although these errors are unrealistically small in our case, for real samples they would be relevant, i.e. they would be larger by a constant factor and data points would be weighted by the same relative weights.

In the cases where the rotation level is very low we proceed in the standard way: we bin the stars in ten equal-number bins along the projected radius R (the distance from the center of the dwarf to the star on the surface perpendicular to the line of sight). The velocity dispersion in each bin is calculated using the standard unbiased estimator of dispersion and assigned a sampling error of size $\sigma/\sqrt{2(n-1)}$ where n is the number of stars per bin.

In the cases when rotation is detected (observation along the x and y axis for model A) we first transform the projected data using the symmetries of the axisymmetric system so that all stars have positive coordinates. Then the data are again binned along the projected radius R . The measured velocity dispersion profiles are plotted as dots as a function of the projected radius R in Figure 9. The sampling errors are not shown because they are very small.

The velocity moments are related to the underlying potential Φ and the distribution of the tracer ν via a set of Jeans equations which in general read (Binney & Tremaine 2008)

$$\frac{\partial}{\partial x_i}(\nu\sigma_{ij}^2) + \nu\frac{\partial\bar{v}_j}{\partial t} + \nu\bar{v}_i\frac{\partial\bar{v}_j}{\partial x_i} = -\nu\frac{\partial\Phi}{\partial x_j}. \quad (4)$$

Together with the continuity equation these equations form a set of four equations relating nine unknown functions, the three components of the mean velocity \bar{v}_j and six components of the symmetric tensor σ_{ij}^2 . The system can only be closed if some additional assumptions are adopted, as in the well-studied cases of spherical symmetry and axisymmetry, which we discuss below. Another

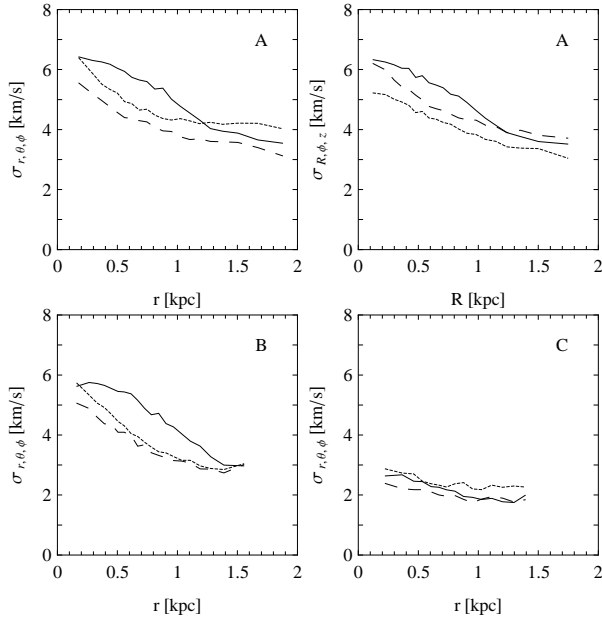


FIG. 10.— The velocity dispersion profiles of the stellar component measured in spherical coordinates r, θ, ϕ in shells containing equal number of stars for models A (upper left panel), B (lower left panel) and C (lower right panel). In each of these panels the solid line refers to σ_r , the dashed line to σ_θ and the dotted line to σ_ϕ . The upper right panel shows the velocity dispersion profiles of the stellar component in dwarf A in cylindrical coordinates R, ϕ and z as a function of R . The solid, dashed and dotted line refers to σ_R , σ_ϕ and σ_z respectively.

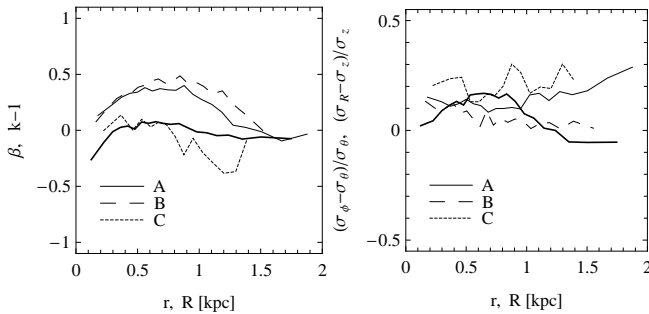


FIG. 11.— Left panel: the spherical anisotropy profiles β of the three simulated dwarfs A, B and C (thin solid, dashed and dotted line respectively) and the axisymmetric anisotropy parameter k (reduced by unity, thick solid line) for dwarf A. Right panel: the relative differences between dispersion profiles $(\sigma_\phi - \sigma_\theta)/\sigma_\theta$ for dwarfs A, B and C (thin solid, dashed and dotted line respectively) and $(\sigma_R - \sigma_z)/\sigma_z$ (thick solid line) for dwarf A.

possibility, for which Jeans equations are solvable, is the case of Stäckel potentials (van de Ven et al. 2003). We find however that none of the well-known triaxial potentials of this form (de Zeeuw et al. 1986) reproduces the density distribution of all our dwarfs. In particular, none of the known models reproduces the rather complicated structure of dwarf A, although the distribution of mass in dwarfs B and C is well fitted by the perfect prolate spheroid (a variation of the so-called perfect ellipsoid, see de Zeeuw 1985). We will further explore the similarities of those dwarfs to the perfect ellipsoid models elsewhere (Łokas et al., in preparation). In any case, with the kind of kinematic samples available for dSph galaxies at present or in the near future there is little

hope of constraining any models beyond spherical or axisymmetric (Statler 1994a,b; van den Bosch & van de Ven 2009).

6.2. Spherical models

We first model only the velocity dispersion profiles using spherical models. For this purpose we solve the lowest order Jeans equation for spherical systems

$$\frac{d}{dr}(\rho\sigma_r^2) + \frac{2\beta}{r}\rho\sigma_r^2 = -\rho\frac{d\Phi}{dr} \quad (5)$$

where we will assume that mass follows light so $\nu = \rho$ up to a constant factor. The radial velocity dispersion σ_r is related to the angular dispersions σ_θ and σ_ϕ by the anisotropy parameter $\beta = 1 - \sigma_\theta^2/\sigma_r^2$. For simplicity we will consider only models with $\beta = \text{const}$ i.e. given by the distribution function $f(E, L) = f(E)L^{-2\beta}$. Such models require that there is no rotation and $\sigma_\theta = \sigma_\phi$. The actual radial dependence of the dispersions (measured with respect to the mean) σ_r, σ_θ and σ_ϕ on radius is shown in Figure 10 for our dwarfs A, B and C. The corresponding profiles of β , calculated by replacing σ_θ^2 with $(\sigma_\theta^2 + \sigma_\phi^2)/2$, are plotted in the left panel of Figure 11. The right panel of the Figure shows the relative differences $(\sigma_\phi - \sigma_\theta)/\sigma_\theta$. We can see that the condition $\sigma_\theta = \sigma_\phi$ is best obeyed for model B and although β profiles vary slowly with radius, our simulated dwarfs are not strongly anisotropic. We believe this level of anisotropy should have negligible effect on our findings.

For comparison with observations the solutions of equation (5) have to be projected along the line of sight (see e.g. Łokas 2002; Łokas et al. 2005). As demonstrated in Figure 2, our models have mass-to-light density ratio almost constant with radius so in the modeling we assume that the mass follows the distribution of stars. Note that if the dwarfs were not strongly affected by tides or were in isolation, more general models with extended dark matter profiles would be more appropriate (e.g. Łokas 2002; Koch et al. 2007a; Battaglia et al. 2008; Walker et al. 2009c). The 3D distribution of stars can be obtained by deprojection of their surface density distribution. The surface density profiles measured for the observations along the x, y and z axis for models A, B and C are plotted as dots in Figure 12. We have also shown that the density distribution of stars is well approximated by the Plummer law (1). The projected density distribution then has a very simple form

$$\Sigma(R) = 2 \int_R^\infty \frac{\rho(r) r}{\sqrt{r^2 - R^2}} dr = \frac{a^2 M}{\pi(a^2 + R^2)^2}. \quad (6)$$

The fits of this formula to the surface density distributions measured for the three lines of sight are plotted in Figure 12 as solid lines and the fitted scale lengths a are given in each panel of the Figure and in the first nine rows of Table 5. (We actually adjusted 2 parameters, the scale length and the normalization, e.g. the stellar mass, but the latter is not relevant here although it was used in the determination of the half-light radii listed in Table 4. The fits were done with the same weighing scheme as before, only now applied to surface densities.)

Table 6 summarizes the results of fitting the solutions of the Jeans equation (5) (by the standard χ^2 minimization) to the velocity dispersion profiles seen along the $x,$

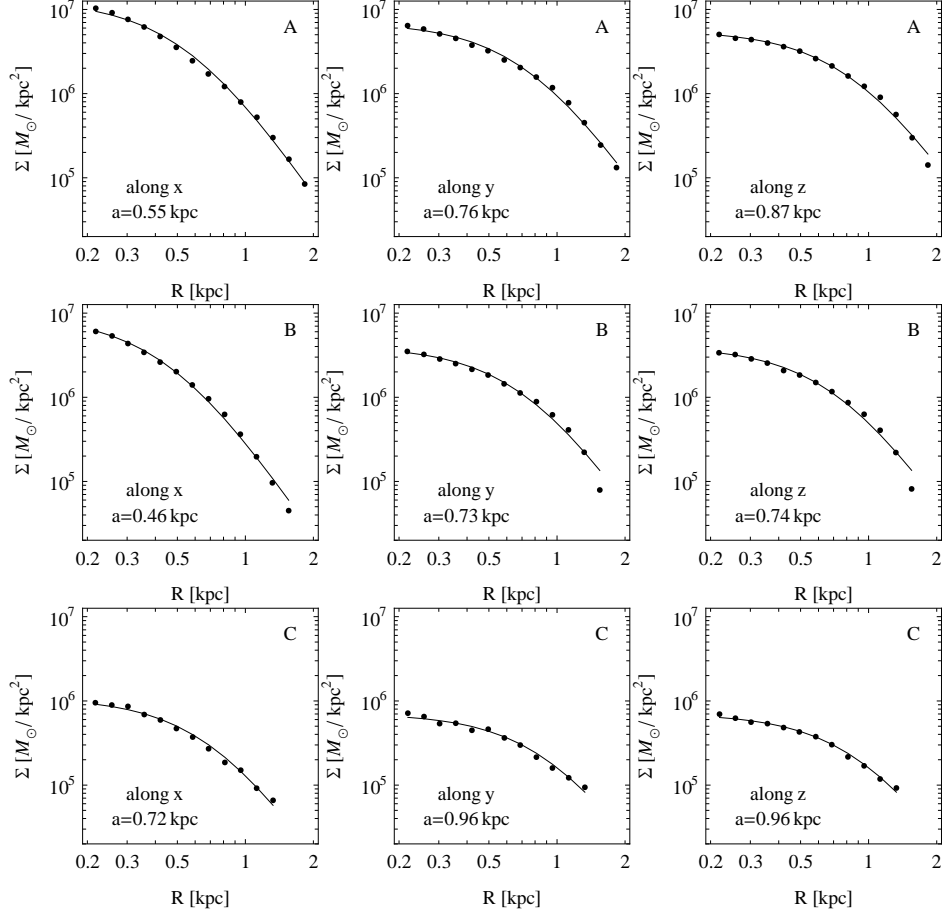


FIG. 12.— Surface density profiles of the stellar component observed along the x , y and z axis (respectively from the left to the right column) for dwarfs formed in simulation A, B and C (from the upper to the lower row). The filled circles show the measurements made along the projected radius R . The solid lines show the best fits obtained with the Plummer surface density profile (6) with parameters listed in Table 5 for the spherical case.

TABLE 5
FITTED PARAMETERS OF THE SURFACE DENSITY PROFILES.

simulation	model	line of sight	a [kpc]	d [kpc]
A	spherical	x	0.55	—
		y	0.76	—
		z	0.87	—
B	spherical	x	0.46	—
		y	0.73	—
		z	0.74	—
C	spherical	x	0.72	—
		y	0.96	—
		z	0.96	—
A	axisymmetric	x	0.56	0.77
		y	0.89	1.89
		z	0.89	1.89

y and z axis for models A, B and C. In each row of the Table the values of the parameters that are kept fixed are given in boldface. We adopted three approaches. First, assuming the shape of the mass profile given by the fitted scale lengths a we adjusted the solutions of the Jeans equation for the isotropic case (with the anisotropy parameter $\beta = 0$) i.e. fitting only the total mass M . The corresponding solutions are plotted as dotted lines in Figure 9. The sixth column of Table 6 gives the masses within $r < r_{\max}$ divided by the actual mass of our sim-

ulated dwarfs within this radius. The last column lists the values of the goodness-of-fit measure χ^2/N rescaled to values corresponding to the total sample of a thousand stars and a hundred stars per bin. Next, keeping the a value fixed we adjust M and β as free parameters. The corresponding solutions are plotted in Figure 9 as solid lines. A third option is to keep $\beta = 0$ and adjust M and the scale length a . The resulting solutions are plotted in Figure 9 as dashed lines. We can see that in most cases by including one more parameter beside the mass we can significantly improve the quality of the fits. Note that β and a cannot both be constrained because they are strongly degenerate with each other, but any of these parameters improves the fits since they both control the shape of the dispersion profiles while the mass acts as a normalization.

The mass of dwarf A is underestimated in all approaches, the least so when the line of sight is along the longest axis. This is obviously due to neglecting the rotation and fitting only the dispersion profiles. This problem can only be self-consistently solved by considering axisymmetric models with intrinsic rotation, as we do in the next subsection. The best-fitting anisotropy is zero to mildly radial in rough agreement with the average value measured in 3D for this dwarf $\beta = 0.22 \pm 0.16$ where the uncertainty is the dispersion of β values in

TABLE 6
FITTED PARAMETERS OF THE SPHERICAL MODELS.

simulation	line of sight	a [kpc]	β	$M[10^7 M_\odot]$	$\frac{M_{\text{fit}}}{M_{\text{true}}}(r_{\text{max}})$	χ^2/N
A	x	0.55	0	3.80	0.91	0.90
		0.55	0.0020	3.80	0.91	1.02
		0.70	0	4.41	0.99	0.84
	y	0.76	0	3.25	0.71	0.45
		0.76	-0.051	3.25	0.71	0.48
		0.96	0	3.76	0.74	0.35
	z	0.87	0	3.19	0.66	0.41
		0.87	0.20	3.26	0.67	0.05
		0.61	0	2.67	0.63	0.03
B	x	0.46	0	2.35	1.03	0.94
		0.46	0.26	2.45	1.07	0.34
		0.29	0	1.93	0.90	0.15
	y	0.73	0	2.11	0.80	0.63
		0.73	0.22	2.16	0.82	0.13
		0.48	0	1.73	0.75	0.07
	z	0.74	0	2.12	0.80	1.12
		0.74	0.30	2.20	0.83	0.20
		0.42	0	1.63	0.73	0.09
C	x	0.72	0	1.02	1.56	1.27
		0.72	-0.20	1.04	1.59	1.10
		1.65	0	1.97	1.20	0.40
	y	0.96	0	0.92	1.13	0.40
		0.96	-0.078	0.92	1.13	0.39
		1.43	0	1.23	0.94	0.24
	z	0.96	0	0.48	0.59	0.85
		0.96	0.24	0.47	0.58	0.31
		0.59	0	0.36	0.61	0.34

NOTE. — The goodness-of-fit measures χ^2/N are rescaled to values corresponding to a total sample of a thousand stars with a hundred stars per bin. The fixed parameters are given in boldface.

the left panel of Figure 11. For dwarf B the mass is typically overestimated when the dwarf is observed along the longest axis and underestimated if seen along any other axis. Note that only in this case the fitted anisotropy is mildly radial for all lines of sight and in good agreement with the 3D value of $\beta = 0.33 \pm 0.14$. This is probably due to the fact that for this case the condition $\sigma_\theta = \sigma_\phi$ required by the spherical models is best fulfilled (see Figure 10 and the right panel of Figure 11). For dwarf C the mass is strongly overestimated when the dwarf is observed along the longest axis and underestimated along the shortest axis. The inferred anisotropy varies from mildly tangential to mildly radial, while the 3D value is $\beta = -0.08 \pm 0.17$. In this case the estimates are least reliable as expected from the highly perturbed state of this dwarf. Note that the best-fitting values of a differ significantly from the ones obtained by fitting the surface density profiles of the stars (Table 5). This approach would therefore only be justified if the density profiles were unknown or highly uncertain. However, the trends in mass estimates are similar to the case when a are fixed and anisotropy is fitted instead. With just three cases analyzed, out of which only one (dwarf B) is really reliable (dwarf A has significant rotation and dwarf C is close to disruption) we cannot draw any firm conclusions concerning the reliability of our estimates of β . However, the trend of mass estimates increasing with line of sight closer to the major axis is clear in all cases.

6.3. Axisymmetric models

So far we have modeled only the line-of-sight velocity dispersion profiles assuming that the galaxy is spherical. We will now try to reproduce both the rotation velocity profile and the velocity dispersion for our dwarf A and those lines of sight where the rotation was detected (observation along the x and y axis). Both moments are shown as a function of the distance along the major axis of the galaxy image in Figure 13. For the fitting the mean velocities were assigned standard errors of the mean σ/\sqrt{n} . For the purpose of this study we will assume that the galaxy can be approximated as an axisymmetric system and again that the mass distribution follows that of stars. Given that the flattening in our simulated dwarfs is much more pronounced in the stellar component (see Figure 1 and fig. 13 in Klimentowski et al. 2009a) than in the dark halo (which remains almost spherical: the densities measured along the major and the minor axis never differ by more than a factor of two) it does not seem to be a realistic assumption. However, such one-component models may still be able to reproduce data better than spherical models.

For the axisymmetric systems it is convenient to work in cylindrical coordinates (R, ϕ, z) where R is now the radial coordinate measured from the center of the galaxy in the equatorial plane. We will assume that the only streaming motion in the galaxy is the rotation so $\overline{v_R} = \overline{v_z} = 0$, $\overline{v_\phi} \neq 0$. If we further assume that the system is described by a distribution function that depends only

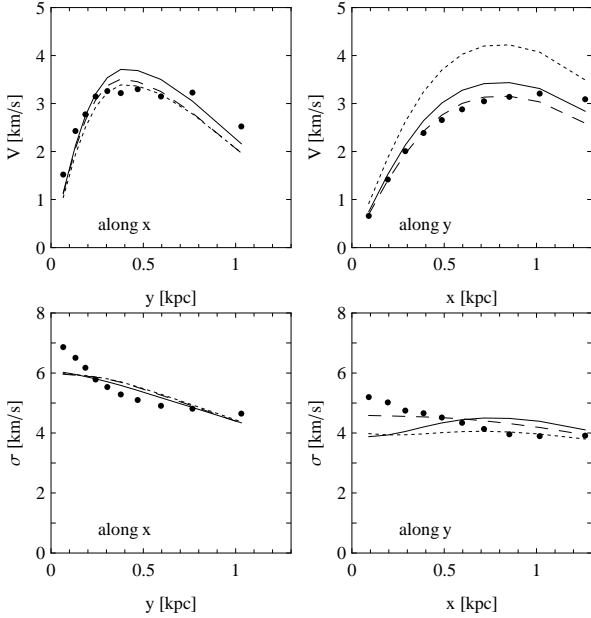


FIG. 13.— The rotation curves (upper row) and the line-of-sight velocity dispersion profiles (lower row) for the observation along the x and y axis (left and right column respectively) for simulated dwarf A. The dotted lines show the best fitting solutions of the single component isotropic ($k = 1$) models with scale parameters a and d adopted from the surface density distribution of stars and only mass M fitted. The dashed lines correspond to best fitting models with a , d and M fitted. The solid lines are for the fits with M and k as free parameters. The best-fitting parameters are listed in Table 7.

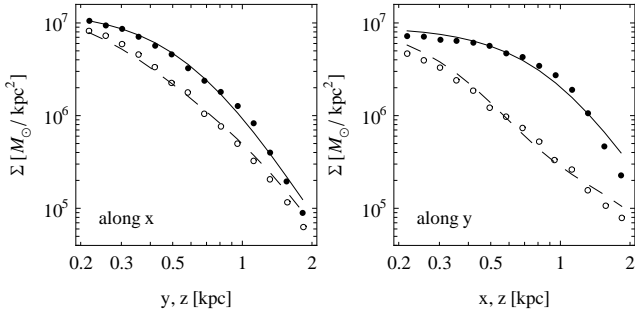


FIG. 14.— Surface density profiles of the stellar component of the dwarf in simulation A seen along the x and y axis (the left and the right panel, respectively). In both panels the filled circles show the measurements made in a strip of width ± 0.2 kpc along the major axis of the image and the open circles the similar measurements along the minor axis. The solid and dashed lines show the best fits obtained with the projected density associated with potential (3) with parameters listed in Table 5 for the axisymmetric case.

on the energy and the z -component of the angular momentum vector, $f = f(E, L_z)$ then the second velocity moments obey $\overline{v_R^2} = \overline{v_z^2}$, the mixed moments vanish and the Jeans equations take the form (Binney & Tremaine 2008)

$$\frac{\partial}{\partial R}(\rho \overline{v_R^2}) + \frac{1}{R} \rho (\overline{v_R^2} - \overline{v_\phi^2}) = -\rho \frac{\partial}{\partial R} \Phi \quad (7)$$

$$\frac{\partial}{\partial z}(\rho \overline{v_z^2}) = -\rho \frac{\partial}{\partial z} \Phi. \quad (8)$$

The rotation may be introduced in an arbitrary way, for example we may have (Sato 1980; Binney et al.

1990)

$$\overline{v_\phi^2} = k^2 (\overline{v_\phi^2} - \overline{v_R^2}) \quad (9)$$

where k is the anisotropy parameter and $k = 1$ corresponds to the velocity distribution which is isotropic everywhere in the system, namely $\overline{v_R^2} = \overline{v_z^2} = \overline{v_\phi^2} - \overline{v_\phi^2}$. With this assumption and the known potential and density, equation (8) can be solved for $\overline{v_z^2} = \overline{v_R^2}$ and introduced into equation (7) to obtain the rotation $\overline{v_\phi}$. For comparison with observations all quantities have to be projected along the line of sight (see Sato 1980).

The upper right panel of Figure 10 shows that our simulated dwarf is not strongly anisotropic. In this Figure we plot the profiles of the three velocity dispersions measured in cylindrical shells along R containing equal numbers of stellar particles. We can see that they are very similar. The only significant difference is visible at $R < 1$ kpc where σ_R is somewhat larger than the other two profiles. This is due to the radial motion of the stars in the inner remnant bar. The relative difference between the dispersions of velocities along R and z is further illustrated in the right panel of Figure 11 as the thick solid line. Its positive value means that the underlying condition of our axisymmetric models, $\overline{v_R^2} = \overline{v_z^2}$ is not strictly obeyed. The profile of the anisotropy parameter k (reduced by unity), calculated by replacing $\overline{v_R^2}$ with $(\overline{v_R^2} + \overline{v_z^2})/2$ in equation (9), is plotted as the thick solid line in the left panel of Figure 11.

The density distribution in these axisymmetric systems will be described by the modified Plummer model (3) with $b = c = 0$

$$\Phi(R, z) = -\frac{GM}{[(R^2 + z^2 + a^2)^2 + d^2 z^2]^{1/4}} \quad (10)$$

where $R^2 = x^2 + y^2$, so the model will be fully determined by its total mass M and two scale lengths, a and d . The ratio of the scale lengths d/a controls the amount of flattening and rotation in the system. We will again start with isotropic ($k = 1$) models where the only free parameter is the mass, while the scale-lengths are determined from the surface density distribution of the stars. To get them we measure the surface density but this time separately along the major and minor axis of the galaxy image. The results for the two lines of sight are illustrated in Figure 14. These profiles were fitted with the projections of the density following from (10) and the resulting scale-lengths a and d are listed in the two lower rows of Table 5. The quality of the fit is much better for the observation along x (left panel of Figure 14) than for the observation along y . This is not surprising since in the latter case the bar is more pronounced.

We proceed to solve the Jeans equations for an axisymmetric system and fit the solutions to the rotation curves and velocity dispersion profiles measured along the x and y axis and plotted in Figure 13. Table 7 summarizes the results. As for the spherical models, the fixed values of the parameters are given in boldface and the χ^2/N values are rescaled to correspond to realistic samples. The Table lists values obtained for different assumed inclinations of the galaxy where i is the angle between the rotation plane and the line of sight. The best-fitting profiles of the velocity moments for $i = 0^\circ$ are plotted in Figure 13. Again, we tried three approaches, starting with

TABLE 7
FITTED PARAMETERS OF THE AXISYMMETRIC MODELS FOR SIMULATION A.

line of sight	i [deg]	a [kpc]	d [kpc]	k	M [$10^7 M_\odot$]	$\frac{M_{\text{fit}}}{M_{\text{true}}}(r_{\text{max}})$	χ^2/N	
x	0	0.56	0.77	1	4.42	1.03	0.74	
	0	0.56	0.77	1.08	4.52	1.05	0.63	
	0	0.54	0.76	1	4.31	1.01	0.81	
	10	0.56	0.77	1	4.43	1.03	0.76	
	10	0.56	0.77	1.09	4.54	1.06	0.61	
	10	0.54	0.77	1	4.31	1.01	0.81	
	20	0.56	0.77	1	4.46	1.04	0.82	
	20	0.56	0.77	1.12	4.60	1.07	0.56	
	20	0.54	0.79	1	4.35	1.02	0.82	
	30	0.56	0.77	1	4.50	1.05	1.00	
	30	0.56	0.77	1.18	4.70	1.09	0.49	
	30	0.53	0.84	1	4.44	1.04	0.84	
	40	0.56	0.77	1	4.57	1.06	1.45	
	40	0.56	0.77	1.28	4.85	1.13	0.40	
	40	0.53	0.90	1	4.60	1.07	0.90	
	50	0.56	0.77	1	4.62	1.08	2.39	
	50	0.56	0.77	1.46	5.04	1.17	0.32	
	50	0.52	0.98	1	4.85	1.13	1.07	
	y	0	0.89	1.89	1	4.38	0.81	3.85
		0	0.89	1.89	0.84	4.11	0.76	2.28
0		0.95	1.39	1	4.58	0.85	0.62	
10		0.89	1.89	1	4.42	0.81	3.76	
10		0.89	1.89	0.84	4.14	0.76	2.25	
10		0.95	1.40	1	4.60	0.86	0.63	
20		0.89	1.89	1	4.52	0.83	3.44	
20		0.89	1.89	0.85	4.25	0.78	2.15	
20		0.95	1.45	1	4.65	0.86	0.64	
30		0.89	1.89	1	4.70	0.87	2.84	
30		0.89	1.89	0.87	4.46	0.82	1.95	
30		0.95	1.53	1	4.78	0.88	0.68	
40		0.89	1.89	1	4.98	0.92	1.98	
40		0.89	1.89	0.91	4.81	0.89	1.65	
40		0.95	1.67	1	5.02	0.91	0.76	
50		0.89	1.89	1	5.36	0.99	1.20	
50		0.89	1.89	0.99	5.34	0.98	1.26	
50		0.95	1.85	1	5.45	0.98	0.96	

NOTE. — The goodness-of-fit measures χ^2/N are rescaled to values corresponding to a total sample of a thousand stars with a hundred stars per bin. The fixed parameters are given in boldface.

fitting the mass only with a and d adopted from the fit to the surface density profile and $k = 1$. The best-fitting solutions are plotted in Figure 13 as dotted lines.

The fits are quite good in the case of the observation along the x axis but rather poor in the case of observation along the y axis, especially for the rotation curve. The rotation is much too large compared to the data in spite of fitting the mass. This overshooting of rotation is due to a very large d/a ratio coming from the fit of the surface density distribution of the stars. In other words, self-consistent axisymmetric and isotropic models would predict more rotation for these d/a ratios. Still, the masses within r_{max} found in this case are reasonable (see Table 7), i.e. they are underestimated by no more than 20 per cent.

As for spherical models we next relax the assumption of isotropy and fit the data again with two free parameters, M and k . As discussed in detail by Binney et al. (1990), decreasing k can suppress the rotation curve of the models while increasing the dispersion profile. The results of the fitting are plotted in Figure 13 as solid lines. As expected, the quality of the fits is now improved, especially

for the observation along the y axis (right hand panels of Figure 13) where the rotation curve is now in better agreement with the data. Note however, that the velocity dispersion profile is now worse reproduced and also the masses within r_{max} are even more underestimated in comparison with the true values. A better approach in this case may therefore be to keep $k = 1$ and adjust a and d instead together with the mass. The corresponding profiles of the velocity moments are plotted in Figure 13 as dashed lines. The fits are now considerably improved and the masses are not underestimated by more than 15 per cent. Note also that the fitted values of a and d are not very different from those estimated from fitting the surface density distribution of the stars.

Figure 15 shows the surface density contours and the line-of-sight kinematics of these best-fitting axisymmetric models in a way analogous to Figures 5 and 8. We can see that the models qualitatively reproduce the shapes and kinematics of the simulated dwarf A. In particular, they reproduce the faster variation of the velocity moments with projected distance when the dwarf is seen along the longest axis, compared to the perpendicular di-

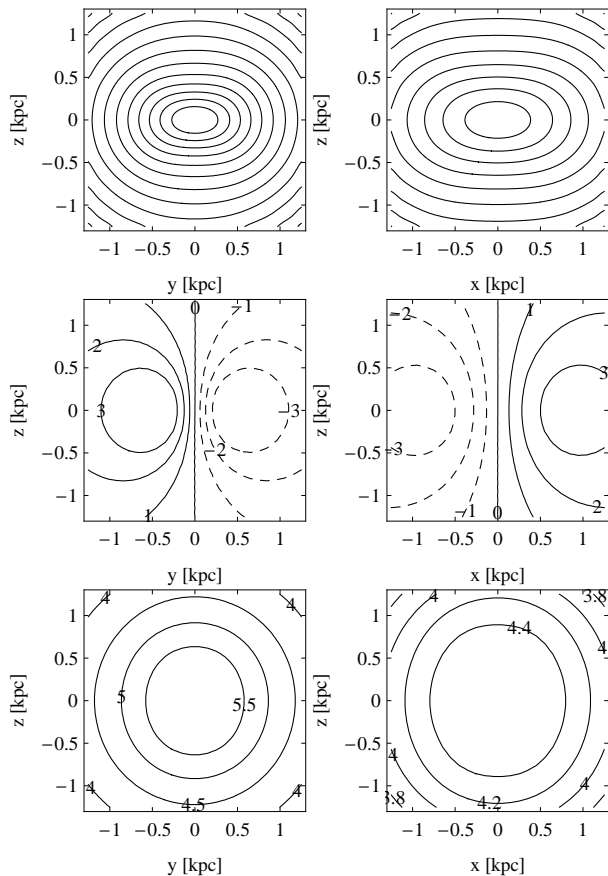


FIG. 15.— The structure and kinematics of the best fitting axisymmetric models for the observation along the x (left column) and y axis (right column) with fitted parameters a , d and M listed in Table 7 assuming inclination $i = 0^\circ$. The upper row panels show the contours of the surface density Σ in $M_\odot \text{ kpc}^{-2}$ plotted at $\Delta \log \Sigma = 0.2$ with the innermost contours corresponding to $\log \Sigma = 7.6$ (left column) and 7.2 (right column). The middle and lower row panels show the contours of the line-of-sight velocity and velocity dispersion respectively, with contour levels in km s^{-1} indicated in each panel. Negative velocity contours are plotted with dashed lines.

rection. Obviously, they are unable to reproduce the velocity gradient seen along the projected minor axis in the middle panel of the upper row in Figure 8 since this would only be possible with triaxial models (Binney 1985).

7. SUMMARY AND DISCUSSION

Using high-resolution N -body simulations we have studied the stellar properties of dSph galaxies resulting from the tidally induced morphological transformation of disk dwarfs on a cosmologically motivated eccentric orbit around the Milky Way. We find that although the simulations differed only by the initial inclinations of the disk with respect to the orbital plane (0° , 45° , and 90°), this single parameter change led to significantly dissimilar outcomes. The reason for this is the well-known effect that the tidal force is more effective in removing stars which are on more prolate orbits with respect to the orbital motion (e.g., Read et al. 2006). The dwarf spheroidal galaxies obtained had different masses, density distributions, and velocity structure. Although we have used a most probable orbit of dwarf galaxies in the Local Group (Diemand et al. 2007), the variation of or-

bitary parameters would further differentiate the outcome of the simulations. On more circular orbits the dwarfs would be less affected by impulsive heating at pericenters and therefore we expect them to be less evolved, preserving a more prolate shape and more rotation as in earlier stages of the evolution on our eccentric orbit (see Klimentowski et al. 2009a).

The least evolved dwarf A (with initial inclination of 90°) has an intrinsically triaxial distribution in the stellar component and preserved a fair amount of rotation. The rotation is mostly around the shortest axis. The intermediate case, dwarf B (with initial inclination of 45°), is a prolate spheroid and retained little rotation. The shape of its stellar component is still rather regular and so the dwarf can be considered a relaxed object. The most strongly evolved dwarf C (with initial inclination of 0°) is also a prolate spheroid with very little rotation but its noisy density contours and profiles of velocity moments indicative of small numbers of bound stars suggest that it is very close to disruption.

Despite the aforementioned differences and the fact that the final masses of the simulated dwarfs differ significantly (see Table 1 and Figure 2), the final M/L ratios are quite similar and fairly constant with radius. The former is related to the fact that the initial mass-to-light distributions of the dwarfs were identical and indicates that the dark matter and stars are lost in proportional amounts in all cases. The latter is a consequence of both our choice of initial conditions for the dwarf galaxy models and the fact that most of the dark matter outside of the stellar component is stripped efficiently. Indeed, in the present study we adopt the Mo et al. (1998) scalings which connect the angular momentum/size of the disk with those of the parent dark matter halo. These general scalings together with our specific choice of parameters result in an initial dwarf galaxy with a M/L ratio which is constant within 2 kpc or so and increases thereafter (Klimentowski et al. 2007). As the outer dark matter halo gets tidally stripped, the effect of increasing M/L ratio at larger distances, characteristic of the initial conditions, disappears. However, it is not difficult to imagine scenarios where this situation can change as, for example, in cases where the original disk dwarfs are constructed with much smaller scale lengths compared to the scale radius of the parent halo, r_s . Such modeling would probably result in a non-constant M/L ratio within the luminous radius of the dwarf as the outer dark matter halo is tidally truncated. Until cosmological simulations reveal the structure of the dwarf progenitors themselves, the choice of initial structural parameters will remain somewhat arbitrary.

We studied the density distribution of the stellar component both radially averaged and along the principal axes. In the former case it is well fitted by the Plummer law, in agreement with real dSph galaxies. For the latter we proposed a simple formula for the potential of the stellar component of the simulated dwarfs based on the generalization of the Plummer law. This formula reproduces quite well the triaxial shape of model A and prolate spheroidal shapes of models B and C (with a smaller number of parameters in the latter cases) both when measured along the principal axes and in projection. The surface density distributions are quite similar to the observed ones, although a detailed comparison is

beyond the scope of the present paper.

We also investigated the velocity distribution of the stars in the dwarfs along the principal axes and along the line of sight. The velocity structure seems to be the richest in the case of model A due to its triaxiality. In this case we detect rotation both around the short and the long axis which manifests itself in the misalignment of the zero velocity curve with respect to the projected minor axis. The velocity structure is much simpler in dwarfs B and C since almost no net streaming motion is seen there. In all models the dispersion of velocity is largest for velocities along the major axis which is due to the origin of the shapes of the dwarfs. All of them went through a prolonged bar-like phase where radial orbits along the bar are dominant and were transformed into prolate spheroids by systematic shortening of the bar.

The projected velocity dispersions of our simulated galaxies decline slowly with radius, although some exhibit larger gradients. This behavior agrees with the observed profiles in real dSph galaxies (e.g. Lokas et al. 2008; Lokas 2009) when the samples are cleaned of contamination using algorithms such as the one described in Klimentowski et al. (2007). Note that the majority of velocity dispersion profiles published in the literature (e.g. Muñoz et al. 2005; Koch et al. 2007b; Walker et al. 2007) are rather flat, which in our opinion is probably due to contamination from the Milky Way or tidally stripped stars but may also be caused by multiple stellar populations (Battaglia et al. 2006) or an extended dark matter component (e.g. Walker et al. 2006).

This velocity structure has important consequences for mass modeling. We fitted the line-of-sight velocity dispersion profiles of the dwarfs observed along the principal axes using different sets of free parameters. When the observation is done along the longest axis (the velocity dispersion is then larger and declines more steeply with radius) the mass is typically mildly overestimated. When it is done along the intermediate or short axis, it is underestimated.

The effect is largest for dwarf C, which is close to disruption, but even in this case the mass is over/underestimated by only about 60 percent. This suggests that the very high mass-to-light ratios estimated for some dSph galaxies, such as Draco or Ursa Major, cannot be explained by departures from sphericity, but are rather the result of the formation process of their progenitors, or are caused by other mechanisms that affected their baryonic mass fraction such as photoevaporation of the gas after reionization (e.g. Babul & Rees 1992; Bullock et al. 2000) or the combined effect of heating by the UV background and subsequent ram pressure stripping in the hot gaseous corona of the Milky Way (Mayer et al. 2006; 2007).

For dwarf B, which seems to provide the best model for the real dSph galaxies (it still has a regular structure and shows little rotation) we find that spherical modelling may overestimate the mass by up to 7 percent (when the line of sight is along the major axis) but underestimate it by up to 27 percent (when viewed along a short axis). Large kinematic samples of a few hundred up to a few thousand stars with measured velocities recently obtained by Walker et al. (2009b) for Carina, Fornax, Sculptor and Sextans allow for mass determinations with statistical errors as small as 5-15 percent

(Lokas 2009) using simple models (assuming constant mass-to-light ratios and anisotropy) described here or similar. This means that the systematic errors due to non-sphericity of dSph galaxies are comparable or larger than the statistical errors in mass determination due to sampling errors of velocity moments for the best-studied dwarfs.

For dwarf A the velocity moments (the rotation curve and the velocity dispersion profile) are much better reproduced with axisymmetric models constructed under the assumption that only the rotation around the shortest axis is present (i.e. neglecting the rotation around the longest axis). Although the presence of rotation has been reported in a number of dSph galaxies, like Ursa Minor (Hargreaves et al. 1994; Armandroff et al. 1995), Leo I (Sohn et al. 2007), Sculptor (Battaglia et al. 2008), Carina (Muñoz et al. 2006) and recently for more distant ones, Cetus (Lewis et al. 2007) and Tucana (Fraternali et al. 2009), it remains to be seen if such models are applicable to real dSph galaxies as they would require measurements of rotation curves at higher significance level than presently available.

We have demonstrated that the kinematics of our simulated dwarfs depends sensitively on the line of sight. This has intriguing implications for the missing satellites problem (Klypin et al. 1999; Moore et al. 1999), which is formulated by mapping the observed stellar velocity dispersions of dwarf galaxies to subhalo maximum circular velocities, V_{\max} (see also Klimentowski et al. 2009a). These results imply that because our remnant dwarfs are non-spherical, V_{\max} depends both on the specific model used to fit the potential of the dwarf and the line of sight used to measure stellar velocity dispersions, σ . In our models, the measurement of the central velocity dispersion alone, when done along the longest axis can be higher by 50 percent compared to the perpendicular direction. We note that these findings are only relevant to dSphs that have a moderate mass-to-light ratio like our simulated dwarfs (e.g. Fornax or Leo I). Dwarfs embedded in a much more massive dark matter halo may in principle have a different relation between σ and V_{\max} since the stars could probe a region well inside the radius at which V_{\max} occurs.

Lastly, the findings of the present study demonstrate that for a given orbit and initial density distribution the stellar structure and kinematics of tidally stripped disk dwarfs depend sensitively on the initial inclination of the disk with respect to the orbital plane. Similar conclusions were reached by Mastropietro et al. (2005) using N -body simulations to follow the tidal evolution and harassment of disk galaxies inside a galaxy cluster environment. The models presented in this paper as well as those of Mastropietro et al. (2005) do not include gas.

Mayer et al. (2006, 2007) have shown that gas present in the disk progenitors of dSphs can be either completely stripped (by ram pressure and tides) or partially retained producing periodic bursts of star formation at pericentric passages. The outcome depends sensitively on when the dwarf fell into the primary potential. The discriminating factors are the strength of the cosmic ultraviolet background and the local flux from the primary at the time of infall. In cases when gas is partially retained, it can affect the structural properties of the remnants, favoring a longer lived stellar bar and reducing

tidal mass loss by increasing its central density following a bar-driven gas inflow. This would tend to produce a remnant more similar to that of model A of this paper, i.e. triaxial and with more residual rotation. However, as the gas is consumed and the dwarf becomes devoid of it, further tidal heating may change the internal structure of the dwarf again. Fornax, Carina and Leo I, that had prolonged star formation, may have gone through these different phases. Overall, the inclusion of gas is likely to induce further scatter in the final structural properties of

dwarf galaxies orbiting the Milky Way. We will extend our analysis to gasdynamical models in future work.

The numerical simulations were performed on the zBox2 supercomputer at the University of Zürich. SK is funded by the Center for Cosmology and Astro-Particle Physics at The Ohio State University. This research was partially supported by the Polish Ministry of Science and Higher Education under grant NN203025333.

REFERENCES

- Armandroff, T. E., Olszewski, E. W., & Pryor, C. 1995, *AJ*, 110, 2131
- Babul, A., & Rees, M. J. 1992, *MNRAS*, 255, 346
- Battaglia, G., et al. 2006, *A&A*, 459, 423
- Battaglia, G., Helmi, A., Tolstoy, E., Irwin, M., Hill, V., & Jablonka, P. 2008, *ApJ*, 681, L13
- Binney, J. J. 1985, *MNRAS*, 212, 767
- Binney, J. J., & Tremaine, S. 2008, *Galactic Dynamics* (Princeton: Princeton Univ. Press)
- Binney, J. J., Davies, R. L., & Illingworth, G. D. 1990, *ApJ*, 361, 78
- Blumenthal, G. R., Faber, S. M., Primack, J. R., & Rees, M. J. 1984, *Nature*, 311, 517
- Blumenthal, G. R., Faber, S. M., Flores, R., & Primack, J. R. 1986, *ApJ*, 301, 27
- Bullock, J. S., Kravtsov, A. V., & Weinberg, D. H. 2000, *ApJ*, 539, 517
- Diemand, J., Kuhlen, M., & Madau, P. 2007, *ApJ*, 667, 859
- D’Onghia, E., Besla, G., Cox, T. J., & Hernquist, L. 2009, *Nature*, 460, 605
- de Zeeuw, T. 1985, *MNRAS*, 216, 273
- de Zeeuw, T., Peletier, R., & Franx, M. 1986, *MNRAS*, 221, 1001
- Fraternali, F., Tolstoy, E., Irwin, M. J., & Cole, A. A. 2009, *A&A*, 499, 121
- Ghigna, S., Moore, B., Governato, F., Lake, G., Quinn, T., & Stadel, J. 1998, *MNRAS*, 300, 146
- Gnedin, O. Y., Lee, H. M., & Ostriker, J. P. 1999, *ApJ*, 522, 935
- Grebel, E. K., Gallagher, J. S., & Harbeck, D. 2003, *AJ*, 125, 1926
- Hargreaves, J. C., Gilmore, G., Irwin, M. J., & Carter, D. 1994, *MNRAS*, 271, 693
- Hernquist, L. 1993, *ApJS*, 86, 389
- Kazantzidis, S., Magorrian, J., & Moore, B. 2004a, *ApJ*, 601, 37
- Kazantzidis, S., Mayer, L., Mastroiello, C., Diemand, J., Stadel, J., & Moore, B. 2004b, *ApJ*, 608, 663
- Klimontowski, J., Lokas, E. L., Kazantzidis, S., Prada, F., Mayer, L., & Mamon, G. A. 2007, *MNRAS*, 378, 353
- Klimontowski, J., Lokas, E. L., Kazantzidis, S., Mayer, L., & Mamon, G. A. 2009a, *MNRAS*, 397, 2015
- Klimontowski, J., Lokas, E. L., Kazantzidis, S., Mayer, L., Mamon, G. A., & Prada, F. 2009b, *MNRAS*, in press, arXiv:0908.4022
- Klimontowski, J., Lokas, E. L., Knebe, A., Gottlöber, S., Martínez-Vaquero, L. A., Yepes, G., & Hoffman, Y. 2009c, *MNRAS*, submitted, arXiv:0909.1916
- Klypin, A., Kravtsov, A. V., Valenzuela, O., & Prada, F. 1999, *ApJ*, 522, 82
- Klypin, A., Zhao, H., & Somerville, R. S., 2002, *ApJ*, 573, 597
- Koch, A., Wilkinson, M. I., Kleyna, J. T., Gilmore, G. F., Grebel, E. K., Mackey, A. D., Evans, N. W., Wyse, R. F. G. 2007a, *ApJ*, 657, 241
- Koch, A., Kleyna, J. T., Wilkinson, M. I., Grebel, E. K., Gilmore, G. F., Evans, N. W., Wyse, R. F. G., & Harbeck, D. R. 2007b, *AJ*, 134, 566
- Kormendy, J. 1985, *ApJ*, 295, 73
- Kormendy, J., Fisher, D. B., Cornell, M. E., & Bender, R. 2009, 182, 216
- Kravtsov, A. V., Gnedin, O. Y., & Klypin, A. A. 2004, *ApJ*, 609, 482
- Lewis, G. F., Ibata, R. A., Chapman, S. C., McConnachie, A., Irwin, M. J., Tolstoy, E., & Tanvir, N. R. 2007, *MNRAS*, 375, 1364
- Lynden-Bell, D. 1962, *MNRAS*, 123, 447
- Lokas, E. L. 2002, *MNRAS*, 333, 697
- Lokas, E. L. 2009, *MNRAS*, 394, L102
- Lokas, E. L., Mamon, G. A., & Prada, F. 2005, *MNRAS*, 363, 918
- Lokas, E. L., Klimontowski, J., Kazantzidis, S., & Mayer, L. 2008, *MNRAS*, 390, 625
- Majewski, S. R., Ostheimer, J. C., Patterson, R. J., Kunkel, W. E., Johnston, K. V., & Geisler, D. 2000, *AJ*, 119, 760
- Mastroiello, C., Moore, B., Mayer, L., Debattista, V. P., Piffaretti, R., & Stadel, J. 2005, *MNRAS*, 364, 607
- Mateo, M. L. 1998, *ARA&A*, 36, 435
- Mayer, L., Governato, F., Colpi, M., Moore, B., Quinn, T., Wadsley, J., Stadel, J., & Lake, G. 2001, *ApJ*, 559, 754
- Mayer, L., Mastroiello, C., Wadsley, J., Stadel, J., & Moore, B. 2006, *MNRAS*, 369, 1021
- Mayer, L., Kazantzidis, S., Mastroiello, C., & Wadsley, J. 2007, *Nature*, 445, 738
- Mo, H. J., Mao, S., & White, S. D. M. 1998, *MNRAS*, 295, 319
- Moore, B., Katz, N., Lake, G., Dressler, A., & Oemler, A. 1996, *Nature*, 379, 613
- Moore, B., Ghigna, S., Governato, F., Lake, G., Quinn, T., Stadel, J., & Tozzi, P. 1999, *ApJ*, L19
- Muñoz, R. R., et al. 2005, *ApJ*, 631, L137
- Muñoz, R. R., et al. 2006, *ApJ*, 649, 201
- Navarro, J. F., Frenk, C. S., & White, S. D. M. 1996, *ApJ*, 462, 563
- Peñarrubia, J., Navarro, J. F., & McConnachie, A. W., 2008, *ApJ*, 673, 226
- Read, J. I., Wilkinson, M. I., Evans, N. W., Gilmore, G., & Kleyna, J. T. 2006, *MNRAS*, 366, 429
- Ricotti, M., & Gnedin, N. Y. 2005, *ApJ*, 629, 259
- Sato, C. 1980, *PASJ*, 32, 41
- Sohn, S. T., et al. 2007, *ApJ*, 663, 960
- Stadel, J. G. 2001, PhD thesis, Univ. of Washington
- Statler, T. S. 1987, *ApJ*, 321, 113
- Statler, T. S. 1994a, *ApJ*, 425, 458
- Statler, T. S. 1994b, *ApJ*, 425, 500
- Strigari, L. E., Bullock, J. S., Kaplinghat, M., Simon, J. D., Geha, M., Willman, B., & Walker, M. G. 2008, *Nature*, 454, 1096
- Susa, H., & Umemura, M. 2004, *ApJ*, 610, L5
- Tassis, K., Kravtsov, A. V., & Gnedin, N. Y., 2008, *ApJ*, 672, 888
- Tolstoy, E., Hill, V., & Tosi, M. 2009, *ARA&A*, 47, 371
- van den Bosch, R. C. E., & van de Ven, G. 2009, *MNRAS*, 398, 1117
- van de Ven, G., Hunter, C., Verolme, E. K., & de Zeeuw, P. T. 2003, *MNRAS*, 342, 1056
- Walker, M. G., Mateo, M., Olszewski, E. W., Bernstein, R., Wang, X., & Woodroffe, M. 2006, *AJ*, 131, 2114
- Walker, M. G., Mateo, M., Olszewski, E. W., Gnedin, O. Y., Wang, X., Sen, B., & Woodroffe, M. 2007, *ApJ*, 667, L53
- Walker, M. G., Mateo, M., Olszewski, E. W., Sen, B., & Woodroffe, M. 2009a, *AJ*, 137, 3109
- Walker, M. G., Mateo, M., & Olszewski, E. W. 2009b, *AJ*, 137, 3100
- Walker, M. G., Mateo, M., Olszewski, E. W., Peñarrubia, J., Evans, W. N., & Gilmore, G. 2009c, *ApJ*, 704, 1274
- White, S. D. M. & Rees, M. J. 1978, *MNRAS*, 183, 341